nanomaterials

MDPI

Article

In-Situ Fabrication of g-C_3N_4/ZnO Nanocomposites for Photocatalytic Degradation of Methylene Blue: Synthesis Procedure Does Matter

Shengqiang Zhang [1], Changsheng Su [2], Hang Ren [1], Mengli Li [1,*], Longfeng Zhu [1], Shuang Ge [1], Min Wang [3], Zulei Zhang [1], Lei Li [1,*] and Xuebo Cao [1,*]

1 College of Biological, Chemical Sciences and Engineering, Jiaxing University, 118 Jiahang Road, Jiaxing 314001, China; zsq@yunyaochina.cn (S.Z.); rh136@outlook.com (H.R.); zhulf1988@mail.zjxu.edu.cn (L.Z.); geshuang8@126.com (S.G.); jerry3641172@126.com (Z.Z.)

2 Department of Chemical and Biomolecular Engineering, University of Notre Dame, IN 46556, USA; changsheng.su@cummins.com

3 State Key Laboratory of High Performance Ceramics and Superfine Microstructure, Shanghai Institute of Ceramics, Chinese Academy of Sciences, 1295 Ding-Xi Road, Shanghai 200050, China; xiaomindafeng@163.com

* Correspondence: menglil@mail.zjxu.edu.cn (M.L.); leili@mail.zjxu.edu.cn (L.L.); xbcao@mail.zjxu.edu.cn (X.C.); Tel.: +86-0573-8364-3852 (M.L.)

Received: 28 December 2018; Accepted: 30 January 2019; Published: 6 February 2019

Abstract: The nanocomposite preparation procedure plays an important role in achieving a well-established heterostructured junction, and hence, an optimized photocatalytic activity. In this study, a series of g-C_3N_4/ZnO nanocomposites were prepared through two distinct procedures of a low-cost, environmentally-friendly, in-situ fabrication process, with urea and zinc acetate being the only precursor materials. The physicochemical properties of synthesized g-C_3N_4/ZnO composites were mainly characterized by XRD, UV–VIS diffuse reflectance spectroscopy (DRS), N_2 adsorption-desorption, FTIR, TEM, and SEM. These nanocomposites' photocatalytic properties were evaluated in methylene blue (MB) dye photodecomposition under UV and sunlight irradiation. Interestingly, compared with ZnO nanorods, g-C_3N_4/ZnO nanocomposites (*x*:1, obtained from urea and ZnO nanorods) exhibited weak photocatalytic activity likely due to a "shading effect", while nanocomposites (*x*:1 CN, made from g-C_3N_4 and zinc acetate) showed enhanced photocatalytic activity that can be ascribed to the effective establishment of heterojunctions. A kinetics study showed that a maximum reaction rate constant of 0.1862 min^{-1} can be achieved under solar light illumination, which is two times higher than that of bare ZnO nanorods. The photocatalytic mechanism was revealed by determining reactive species through adding a series of scavengers. It suggested that reactive $\bullet O_2^-$ and h^+ radicals played a major role in promoting dye photodegradation.

Keywords: ZnO nanorods; dye photodegradation; graphitic carbon nitride; nanocomposites; in situ synthesis

1. Introduction

Solar energy is believed to be the most abundant source of sustainable and clean energy [1]. Photocatalysis is a developing green technology that can utilize solar energy for a wide range of applications, such as the decomposition of various organic compounds in water purification processes [2–5], hydrogen production and CO_2 photoreduction in energy conversion [6–8], and bacterial inactivation in medicine [9]. Among well-known semiconductor photocatalysts, ZnO is promising because of its remarkable properties, such as physicochemical/thermal stability, low-cost, high redox potential, and electron

mobility [10–12]. However, its incomplete visible light absorption, poor charge separation, and susceptibility to photo-corrosion have seriously hindered its practical applications. Extensive attention has therefore been made to enhance the photocatalytic activity and stability of ZnO based photocatalysts via heteroatom doping [13–16], novel metal deposition [17,18], or coupling with narrow band gap semiconductors [19–21].

Recently, a light non-metal semiconductor graphitic carbon nitride (g-C_3N_4) has attracted much interest due to its unique electronic structure, remarkable chemical stability, visible light activity, and cost-effective features [22,23]. As a typical analogue of graphite and new photocatalyst, g-C_3N_4 possesses a bandgap of ~2.7 eV, which enables it to be excited by visible light [24]. However, like many other single-component photocatalysts, its quantum efficiency is negatively affected by the fast recombination of photo-generated holes and electrons [25]. Therefore, it still remains a challenge to obtain highly stable and active g-C_3N_4 based photocatalysts.

Coupling g-C_3N_4 with ZnO to form heterostructured nanocomposites presents a novel and feasible route to enhance light sensitivity and charge carrier separation [26]. The improved adsorption of visible light and photocatalytic activity of g-C_3N_4/ZnO nanocomposites could be attributed to the establishment of a heterojunction between g-C_3N_4 and ZnO [26]. In their pioneering studies, Wang et al. [27] and Liu et al. [28] independently synthesized g-C_3N_4 and ZnO heterostructured composites through a two-step chemisorption method [27] and a ball milling method [28]. In a later report, Zhu et al. [29] were the first to introduce the preparation of g-C_3N_4/C-doped ZnO composites through a calcination method. More recently, Wang et al. constructed core-shell g-C_3N_4/ZnO nanocomposites as a photoanode via a reflux method [10], demonstrating enhanced visible-light-irradiated photoelectrocatalytic (PEC) performance for phenol decomposition. One dimensional ZnO nanorods were successfully coated with g-C_3N_4 through reflux and vapor condensation procedures [30], and the photocurrent density of those fabricated 1-D ZnO/g-C_3N_4 composites was approximately 0.12 mA·cm^{-2}.

The nanocomposite preparation procedure plays a crucial role in achieving the well-established heterostructured junction between g-C_3N_4 and ZnO, and hence, an optimized photocatalytic activity [29]. Nevertheless, the synthesis of g-C_3N_4/ZnO nanocomposites usually requires the use of environmentally-unfriendly organic solvents or involves an undesired multi-step synthesis technique. In previous reported studies, the synthesis of ZnO nanorods and g-C_3N_4 were introduced through a facile calcination process [30]. This low-cost, environmentally-friendly method leads to the formation of g-C_3N_4/ZnO nanocomposites through a simple and effective in-situ process. Remarkably, we used urea and zinc acetate as the only precursor materials to synthesize g-C_3N_4/ZnO nanocomposites with a g-C_3N_4:ZnO weight ratio of *x*:1 (*x* = 0.05, 0.1, 0.2 and 0.3) through a two-step in-situ calcination method. Particularly, as illustrated below, g-C_3N_4/ZnO nanocomposites were prepared by using zinc acetate and urea, respectively, as the starting material of the in-situ synthesis process. The specific surface area of these samples increased with the increase of the g-C_3N_4 weight ratio, and the results are shown in Figure S1 and Figure S2.

We explore here the effect the synthesis procedure has on the physiochemistry, photoelectrochemistry (PEC) properties, and photodegradation activities of g-C_3N_4/ZnO nanocomposites (*x*:1 vs. *x*:1 CN) prepared by an in-situ calcination route. Interestingly, in comparison with ZnO nanorods, nanocomposites (*x*:1) exhibited weak photocatalytic activity probably due to the "shading effect" [31,32], while nanocomposites (*x*:1 CN) showed enhanced photodegradation activity due to the effective establishment of heterojunctions [33]. This work is believed to be the first attempt in the field to investigate the effect of g-C_3N_4/ZnO synthesis procedure by in-situ calcination methods. The in-situ calcination approach benefits from low-cost and potential to scale for industrial applications.

2. Materials and Methods

2.1. Catalyst Preparation

Urea and zinc acetate were supplied by Sinopharm Chemical Reagent Co., Ltd (Shanghai, China). Methylene blue, ammonium oxalate (AO), and isopropanol (IPA) were purchased from Aladdin

reagent Co., Ltd (Shanghai, China). All the chemicals were analytical grade and used as received without any further purification.

ZnO nanorods were synthesized by a one-step method described elsewhere [34]. Briefly, 2.94 g zinc acetate dehydrate was added in an agate mortar and grinded for about 30 min. Finally, this grinded powder was put in an alumina crucible and annealed at 350 °C for 3 h with a ramp rate of 5 °C/min. To obtain the g-C_3N_4 powder, an appropriate dose of urea in an alumina crucible was thermally decomposed at 550 °C for 2 h in a muffle furnace (Nabertherm L15, Lilienthal, German) under static air, as described in our previous studies [35].

Scheme 1 illustrates the details of two distinct g-C_3N_4/ZnO synthesis paths. As for *x*:1 samples (*x*:1 represents weight ratio of g-C_3N_4 and ZnO), synthesized ZnO nanorods were grinded and mixed with various amounts of urea, and then annealed with a cover at 550 °C for 2 h.

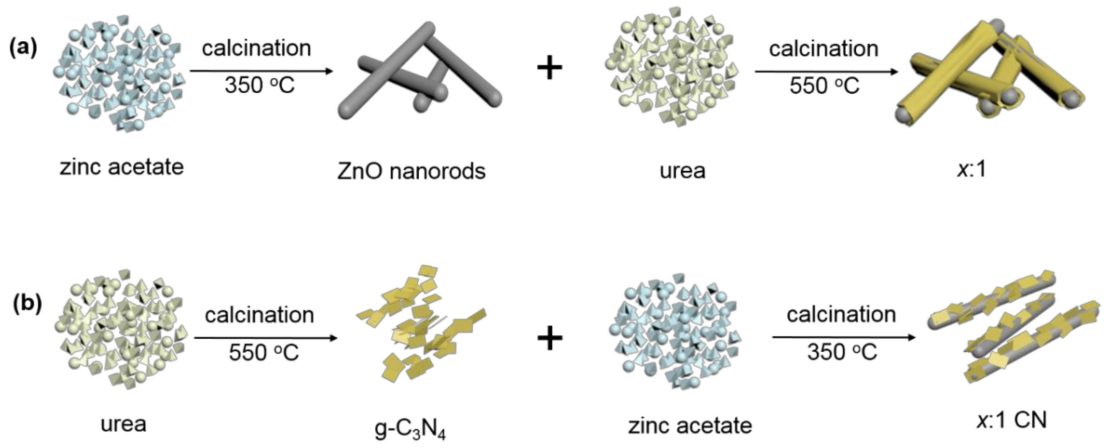

Scheme 1. Schematic rendering of two distinct in-situ synthesis procedures: (**a**): Zinc acetate as the starting precursor (denoted as *x*:1); (**b**) urea as the starting precursor (denoted as *x*:1 CN).

The *x*:1 CN samples were obtained by grinding the necessary amounts of g-C_3N_4 powder mixed with zinc acetate in a quartz mortar. The mixture was then calcinated in a muffle furnace at 350 °C for 3 h and then cooled to room temperature naturally.

2.2. Catalytic Evaluation

Methylene blue (MB, 1×10^{-5} mol/L) photocatalytic degradation was typically conducted in a quartz tube under ultraviolet light (Philips, 18 W) or sunlight (place location: 120.76° in longitude, and 30.77° in latitude), and 50 mg of photocatalyst was dispersed in 100 mL of MB solution each time. The resulting solution was stirred in the dark for 30 min to ensure that the mixture had reached an adsorption and desorption equilibrium, and then the solution was illuminated under stirring. Five milliliters of solution was sampled from the tube at regular intervals and analyzed by UV–visible spectrophotometry (Shimadzu UV-2450). During the stability test, the suspension was centrifuged and washed with deionized water several times for each run. Finally, the powder photocatalyst was collected and dried in an oven in air at 60 °C overnight prior to being used for the next run.

2.3. Characterization

These as-synthesized nanocomposites were studied by various techniques. X-ray powder diffraction (XRD) patterns were collected by a German Bruker D8 Focus Powder (Fremont, CA, USA) using Cu Kα radiation. The scanning speed was setted to 4°/min. The specific surface area of these samples was calculated by the Brunauer–Emmett–Teller (BET) method and characterized by sorption using a Micromeritics Tristar 2000 instrument (Atlanta, GA, USA) at 77 K. Transmission electron microscopy (TEM, JEM-2100F, Tokyo, Japan) and selected area electron diffraction (SAED) patterns were operated at 200 kV. Field emission scanning electron microscopy (FE-SEM) images were

obtained with a Hitachi S-4800 (Tokyo, Japan). UV–visible diffuse reflectance spectroscopy (DRS) was acquired on a UV-3101 PC Shimadzu spectroscope (Kyoto, Japan) at room temperature, and $BaSO_4$ was chosen as reference material. The photoluminescence (PL) spectra were recorded on a Hitachi F-4500 fluorescence spectrometer (Tokyo, Japan). X-ray photoelectron spectroscopy (XPS) was taken on a Thermo Scientific ESCALAB 250 spectrometer (Waltham, MA, USA) with a monochromatic X-ray line source of Al Kα radiation. All the binding energies were calibrated internally by setting C 1s to 284.6 eV. The surface molecular structural was studied by Fourier transform infrared (FTIR) spectroscopy (470 FI-IR, Medison, WI, USA).

3. Results and Discussion

3.1. Physicochemical Properties

The XRD analysis in Figure 1 shows patterns of g-C_3N_4, ZnO, and the nanocomposites synthesized by two distinct in-situ synthesis procedures with different g-C_3N_4:ZnO weight ratios. The nanocomposites prepared with g-C_3N_4 as the starting precursor are denoted as *x*:1 CN. The distinct peak at 2 theta of 13.1° for g-C_3N_4 belonged to the (100), corresponding to in-plane packing motif, and the other one at 27.4° originated from the (002) stacking structure [36]. Likewise, the distinct diffraction peaks at 2 theta of 31.8°, 34.0°, 36.3°, 47.5°, 56.9°, 62.9°° and 68.0° for pure ZnO indicated its hexagonal structure (JCPDS No. 36-1451). When using zinc acetate as the starting precursor, the g-C_3N_4 phase could not be detected until the g-C_3N_4 weight ratio in nanocomposite was greater than 0.1:1. In contrast, there was no evidence of g-C_3N_4 crystalline formation, even with the increase of g-C_3N_4 content when using urea as the starting precursor, which can be ascribed to the high dispersion of g-C_3N_4.

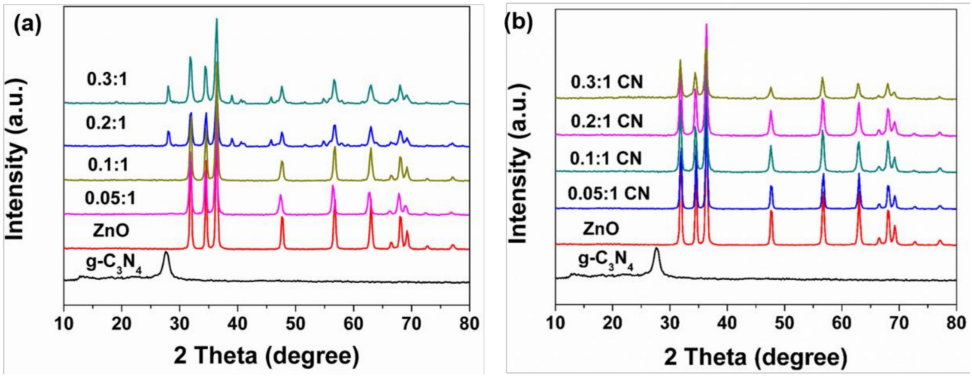

Figure 1. XRD patterns of pure g-C_3N_4, as-prepared ZnO nanorods, with (**a**): g-C_3N_4/ZnO (*x*:1), and (**b**) g-C_3N_4/ZnO (*x*:1 CN).

SEM images depicted in Figure 2 are ZnO nanorods, g-C_3N_4/ZnO (0.1:1), and g-C_3N_4/ZnO (0.1:1 CN), respectively. The morphology of as-prepared ZnO nanorods is shown in Figure 2a. The length of these nanorods was in the magnitude of 1 μm, with the diameter of 30–100 nm. After mixing with urea and followed with in-situ calcination, the morphology of formed nanocomposites g-C_3N_4/ZnO (*x*:1) showed that ZnO nanorods were wrapped with g-C_3N_4 resulting from urea thermopolymerization (Figure 2b). In contrast, the morphology of g-C_3N_4/ZnO (0.1:1 CN) showed only moderate coverage of g-C_3N_4 over ZnO nanorods.

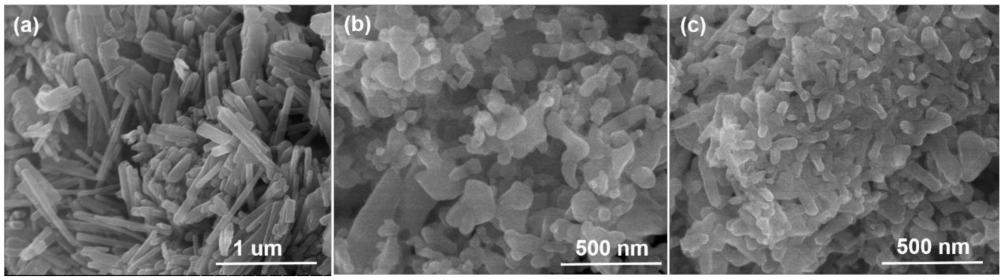

Figure 2. SEM images: (**a**) As-prepared ZnO nanorods; (**b**) g-C_3N_4/ZnO (0.1:1); and (**c**) g-C_3N_4/ZnO (0.1:1 CN).

The morphology of ZnO crystalline and g-C_3N_4/ZnO composites was also investigated by TEM. As can be seen in Figure 3a, the as-prepared ZnO nanorods showed a characteristic rod-shaped crystalline structure, and the corresponding hexagonal crystalline plane (0001) [34] was demonstrated by SAED shown in the inset of Figure 3a. TEM and HRTEM images of g-C_3N_4/ZnO (*x*:1) composites are present in Figure 3c and 3d, suggesting that ZnO nanorods were coarsened after the second step calcination with the presence of urea, and the nanorods were completely covered with g-C_3N_4 even at a g-C_3N_4:ZnO ratio of 0.1:1, which is in accordance with previous SEM observations. In comparison, Figure 3b shows the TEM image of g-C_3N_4/ZnO (*x*:1 CN) nanocomposites, where ZnO nanorods were slightly covered with g-C_3N_4. The EDX images shown in Figure 3e also suggests the homogeneous interaction of g-C_3N_4 with ZnO in the case of g-C_3N_4/ZnO (*x*:1 CN) composites. After 2 h of ultrasonic treatment, there was no evident change in the morphology of g-C_3N_4/ZnO (*x*:1 CN) composites, suggesting a strong combination of g-C_3N_4/ZnO which is shown in Figure S3. The strong interaction between g-C_3N_4 and ZnO is believed to be critical for the efficient formation of heterojunction [27]. The functional groups of ZnO, g-C_3N_4 and their nanocomposites were characterized by FTIR as presented in Figure 4. The peaks at 1637 cm^{-1} and 1243 cm^{-1} are attributed to C=N and C–N stretching in g-C_3N_4 [3], while the peak at 807 cm^{-1} corresponds to the plane breathing vibration [19]. The peaks at 1406, 1450, and 1560 cm^{-1} might be due to heptazine-derived repeating units [10,37].

DRS was performed to study the optical adsorption properties in the range of 200–800 nm for as-prepared ZnO nanorods, g-C_3N_4, and two distinct series of g-C_3N_4/ZnO composite (*x*:1, and *x*:1 CN) samples. As can be seen in Figure 5a and 5b, g-C_3N_4/ZnO nanocomposites prepared by both routes showed good light absorption, signifying their UV and sunlight-induced catalytic activity. Evidently, the absorption edges of all nanocomposites had red-shifted and demonstrated significantly enhanced absorption between 380 nm and 800 nm, when compared with that of bare ZnO nanorods. The g-C_3N_4/ZnO nanocomposites prepared by both routes showed that the absorbance gradually increased with the increase of g-C_3N_4 weight ratio, mainly resulting from a relatively narrow bandgap of g-C_3N_4 which is demonstrated in Figure 5c. The bandgap energy of ZnO and g-C_3N_4 can be calculated using the Kubelka–Munk formula, $(\alpha h\nu)^n = k(h\nu - E_g)$, where E_g is the band gap energy [38]. The extrapolated intercept in Figure 5c gives the corresponding E_g value of 2.88 and 3.07 eV for g-C_3N_4 and ZnO nanorods, respectively.

Photoluminescence (PL) spectroscopy was performed to determine the efficiency of interfacial charge carrier separation in the nanocomposite photocatalysts. It is known that photoluminescence emissions on semiconductors originate from the radiative recombination of photoelectrons and holes [34]. As shown in Figure 5d, bare g-C_3N_4 had a broad PL peak centered at approximately 480 nm. However, the PL results of ZnO and g-C_3N_4/ZnO showed emissions of broad violet (~380 nm) and narrow green-yellow bands (~560 nm). ZnO normally exhibits luminescence in the visible spectral range because of intrinsic or extrinsic defects [39,40]. Previous studies [40] suggest that the defects formed during calcination and can be ascribed to an oxygen vacancy and interstitial oxygen. This was confirmed by XPS as described below. The impurity levels could enhance the photogenerated charge carrier separation in photocatalysts. Therefore, the oxygen defects in ZnO based semiconductors could act as active sites, since the redox reactions usually occur on the surface

of the photocatalyst. The PL emission intensities decreased with the addition of g-C_3N_4 for both cases of g-C_3N_4/ZnO (0.1:1) and g-C_3N_4/ZnO (0.1:1 CN), which is an indication that the recombination of charge carriers in ZnO had been effectively inhibited after the formation of heterojunction structures between g-C_3N_4 and ZnO. The g-C_3N_4/ZnO (0.1:1 CN) composite had the lowest emission intensity, implying its high photocatalytic activity. The presence of g-C_3N_4 lead to promoted electron transfer in the nanocomposites.

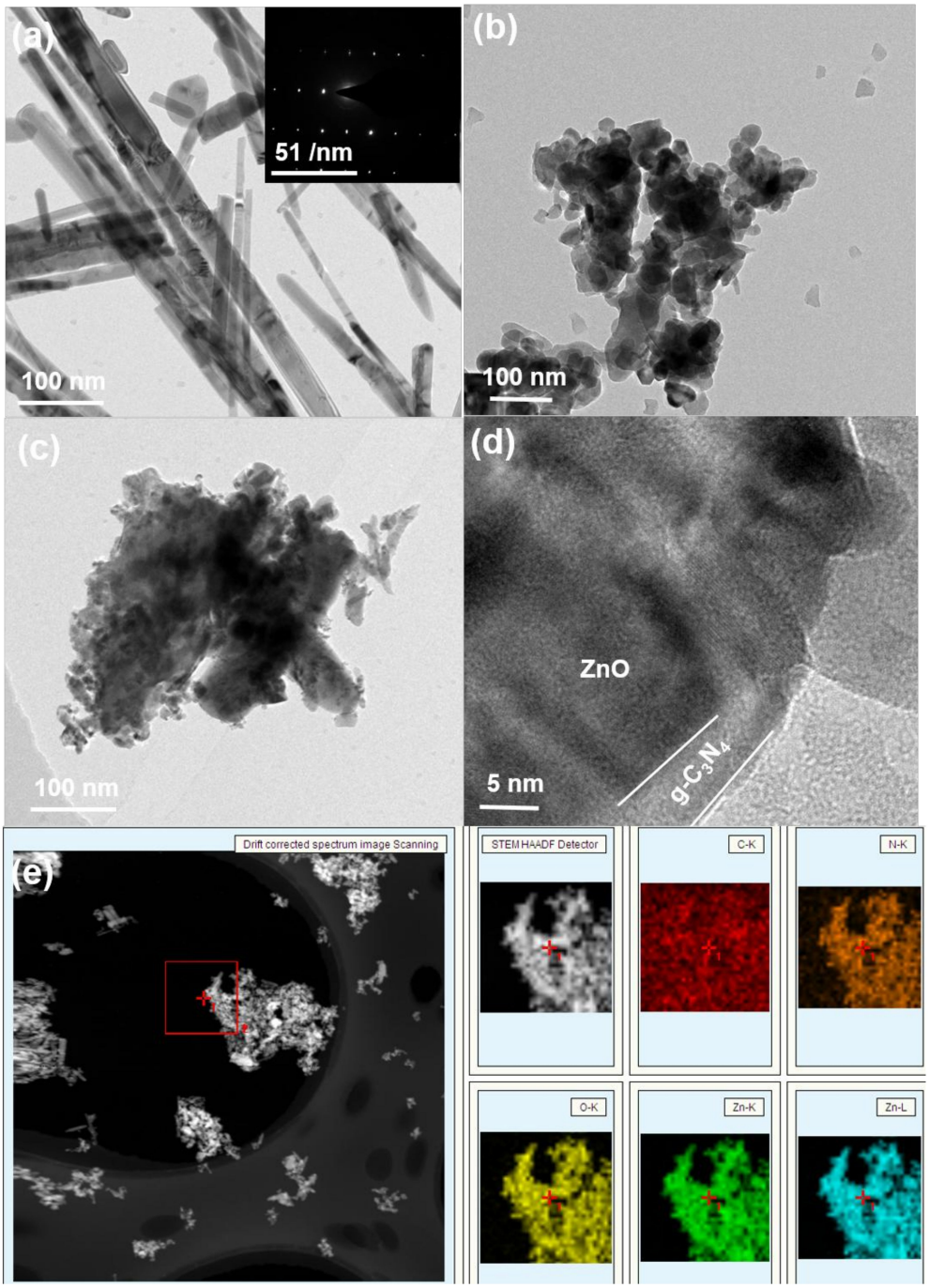

Figure 3. TEM imges of (**a**) ZnO nanorods with inserted selected area electron diffraction (SAED) pattern (inset of (a)), (**b**) 0.1:1 CN, (**c**) 0.1:1, (**d**) HRTEM of 0.1:1, low magnification of 0.1:1 CN and (**e**) the corresponding element mappings.

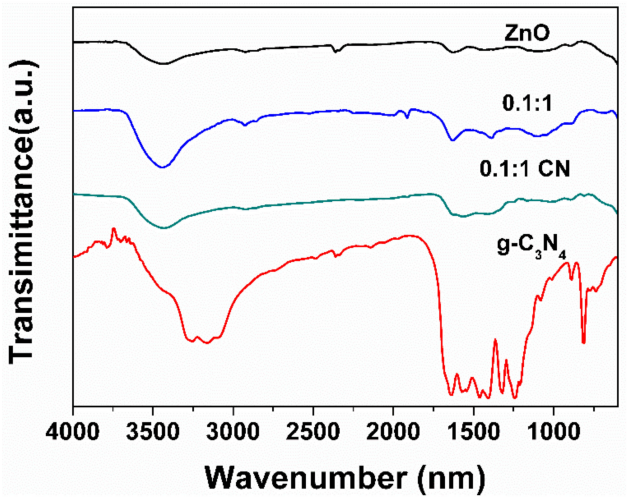

Figure 4. FTIR spectra ZnO, g-C_3N_4 and g-C_3N_4/ZnO nanocomposites synthesized through different procedures.

XPS was conducted to better understand surface species of ZnO nanorods and the nanocomposites. Figure 6a demonstrates that the C 1s spectrum of the composite can be fitted with two peaks at 284.6 eV and 288.4 eV, which correspond to the surface adventitious carbon and the sp^2-bonded C in N=C–N coordination [41]. Unsurprisingly, only adventitious carbon with a peak at 284.6 eV existed in ZnO nanorods. The binding energy values at 532.5 eV, 531.5 eV, and 530.1 eV in O 1s spectra were observed in the heterostructured samples, while three peaks at around 532.4 eV, 531.4 eV and 530 eV existed in ZnO. These peaks can be ascribed to chemisorbed (O_C) oxygen species, oxygen in deficient regions (O_V), and O_2^{2-} species in lattice (O_L) [42]. It is interesting to find that chemisorbed oxygen species also presented in g-C_3N_4/ZnO nanocomposites. These oxygen species are believed to be associated with surface defects [34], implying that g-C_3N_4/ZnO (0.1:1 CN) composite has a high amount of surface defects. Many researchers [25,43] suggest that the differences of photocatalytic activity for different semiconductors result from varying oxygen defect concentrations and types. Furthermore, the oxygen species signal at 532.5 eV was caused by a surface hydroxyl functional group. The N 1s spectrum in Figure 6c can be classified into two peaks. The peak centered at 398.6 eV was attributed to the sp^2-hybridized nitrogen atoms in C=N–C groups [44], while the other one at 400.0 eV was associated with the tertiary nitrogen H–N–C_2 or N–C_3 groups [45]. The Zn 2p spectra were deconvoluted into two peaks of 1021.0 and 1044.0 eV as shown in Figure 6d, corresponding to Zn $2p_{3/2}$ and $2p_{1/2}$, respectively. Compared with pure ZnO, the binding energy of O 1s of g-C_3N_4/ZnO (0.1:1 CN) exhibited a positive shift, while Zn 2p showed a negative shift, suggesting possible chemical bonding formation between ZnO and g-C_3N_4 in the nanocomposite. This interaction was beneficial to promote the charge carrier transfer, and thus enhance photocatalytic activity, which could be further demonstrated by following photocatalytic performance results.

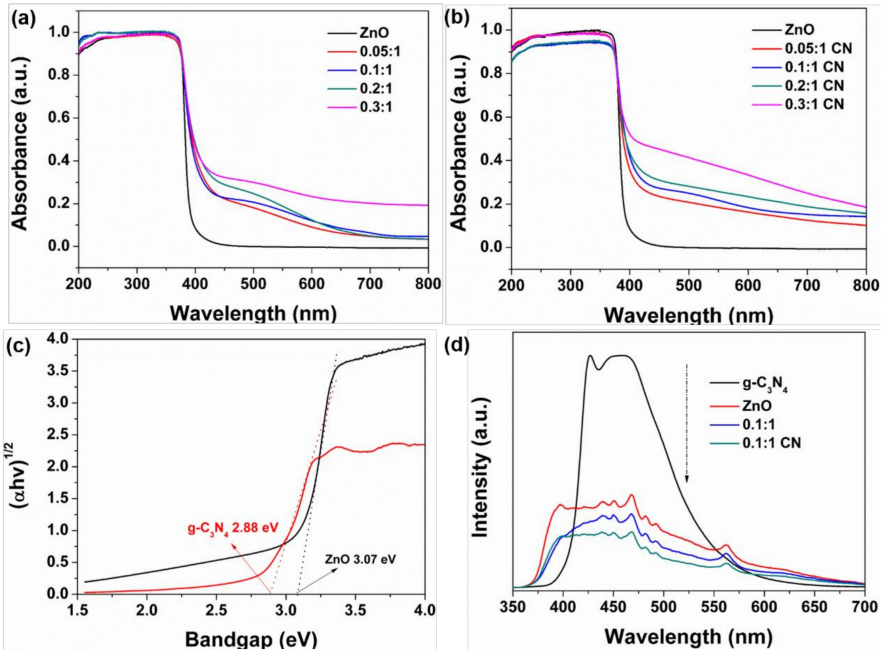

Figure 5. (**a**,**b**) UV–VIS diffuse reflectance spectroscopy (DRS) spectra for ZnO and the g-C_3N_4/ZnO samples, (**c**) the plots of $(\alpha hv)^{1/2}$ versus bandgap of ZnO nanorods and g-C_3N_4, (**d**) photoluminescence (PL) spectra of the prepared photocatalysts.

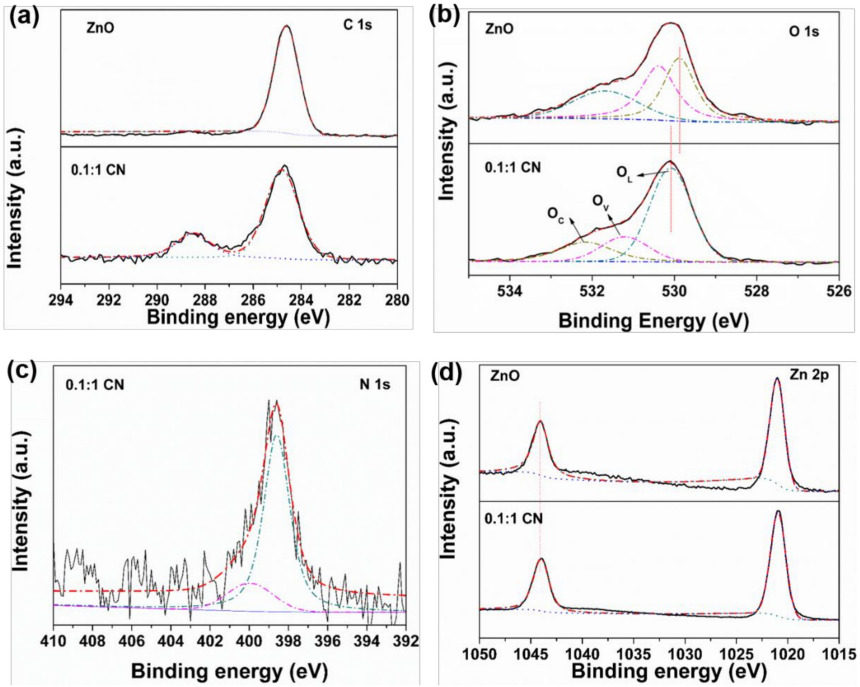

Figure 6. X-ray photoelectron spectroscopy (XPS) data for (**a**) C 1s, (**b**) O 1s, (**c**) N 1s, and (**d**) Zn 2p for the photocatalysts.

3.2. Photocatalytic Performance

The photocatalytic degradation results are shown in Figure 7. No detected degradation was observed without catalyst under light irradiation, which means that the MB was quite stable under this condition. It was found that all nanocomposites (both *x*:1 and *x*:1 CN) exhibited weakened photocatalytic activity under UV light irradiation (Figure 7a,c) compared to that of ZnO. This might have resulted from an enhanced PL phenomenon in g-C_3N_4 and will be further investigated in future

studies. For g-C_3N_4/ZnO (*x*:1) nanocomposites, the photodegradation activity continued to improve with the increase of g-C_3N_4 weight ratio under sunlight irradiation, although they exhibited less activity than that of bare ZnO nanorods. This could be due to the "shading effect" [32], since ZnO nanorods were wrapped by g-C_3N_4 as can be seen from SEM and TEM images. This would result in only the outer g-C_3N_4 being activated by photons and catalytically active during MB photodegradation. In contrast, g-C_3N_4/ZnO (0.1:1 CN) showed the best photocatalytic activity among all g-C_3N_4/ZnO (*x*:1 CN) nanocomposites, which might have resulted from its heterojunction structure leading to low recombination of charge barriers and sufficient active sites. Furthermore, compared to pristine ZnO nanorods, all nanocomposites (both *x*:1 and *x*:1 CN) showed enhanced activity under sunlight irradiation. As shown in Figure 7e, the photocatalytic reaction under sunlight was fit to pseudo-first order kinetics, where the reaction rate constant (k) could be calculated by rate law, $-\ln(C/C_0) = kt$, with C and C_0 being the concentrations of MB. The rate constants were calculated as 0.0901 and 0.1862 min^{-1} for ZnO and g-C_3N_4/ZnO (0.1:1 CN), respectively. The stability of g-C_3N_4/ZnO (0.1:1 CN) was also evaluated (Figure 7f), and there was negligible degradation on the catalytic activity after four repeated cycles, indicating a good promise to potential industrial applications.

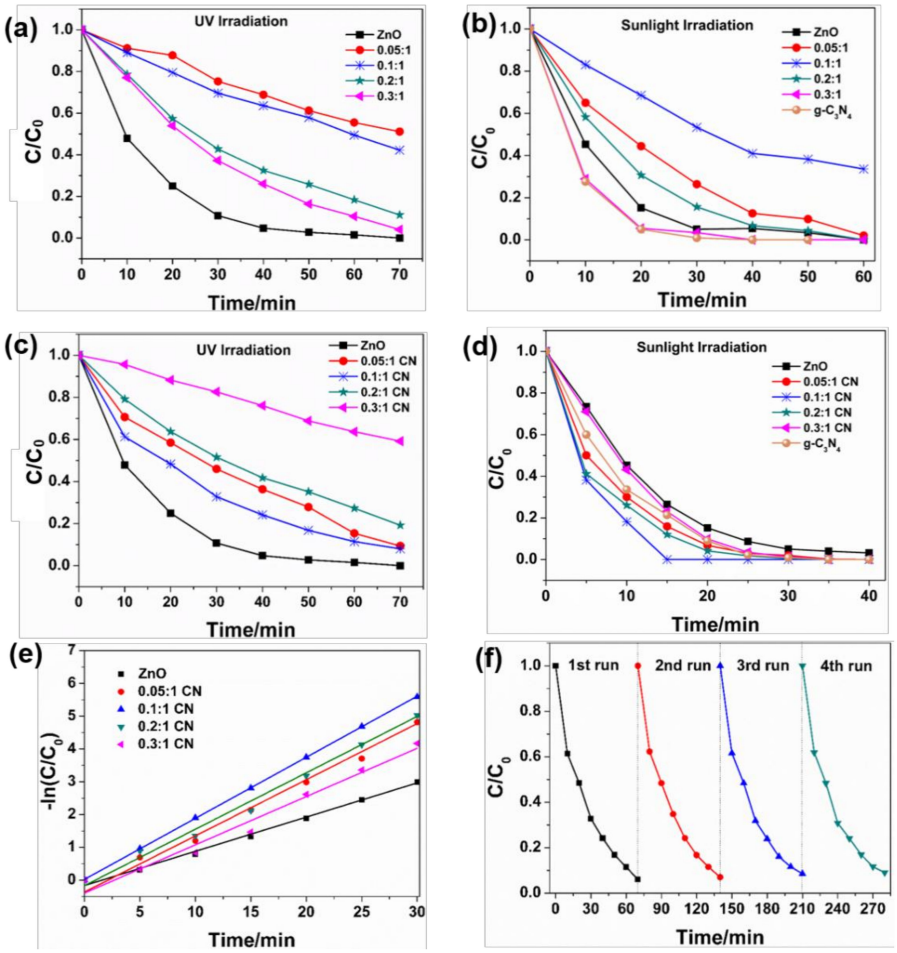

Figure 7. Degradation rate of methyl blue (MB) under ultraviolet (**a**,**c**) and sunlight (**b**,**d**) irradiation, kinetic linear simulation over 0.1:1 CN photocatalyst (**e**) and stability study of MB degradation over 0.1:1 CN.

3.3. Photocatalytic Mechanism

To find out the major active species for the photocatalytic oxidation, several scavengers were added in the photocatalytic system individually to trap and remove corresponding active species. It was reported that ammonium oxalate (AO), isopropanol (IPA), and N_2 could act as effective

scavengers to holes (h^+), hydroxyl radical (•OH), and superoxide radical ($\bullet O_2^-$) [46–59]. As shown in Figure 8, the photodegradation activity of the g-C_3N_4/ZnO (0.1:1 CN) sample had a dramatic decrease with the addition of AO and N_2 under light irradiation, suggesting that both holes and $\bullet O_2^-$ are the main oxidative species in a MB degradation reaction. Moreover, the photocatalytic activity decrease was greater in the presence of N_2, indicating that the $\bullet O_2^-$ species was more active than holes during the photodegradation process. On the other hand, the introduction of IPA did not have a noticeable impact on the photocatalytic activity, implying that •OH did not play a significant role in the reaction as an oxidative species.

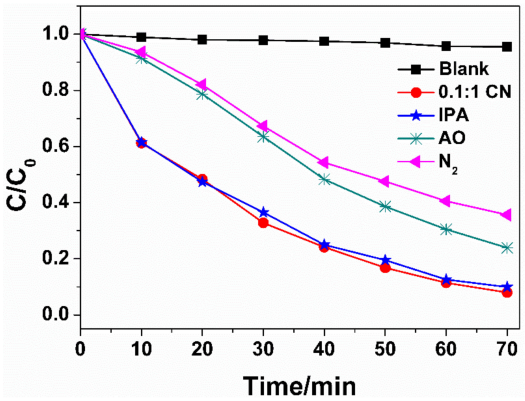

Figure 8. Effect of several scavengers on the photocatalytic activity of 0.1:1 CN sample.

4. Conclusions

A series of g-C_3N_4/ZnO nanocomposites were prepared through two distinct procedures of the in-situ fabrication process. In comparison with ZnO nanorods, g-C_3N_4/ZnO nanocomposites (*x*:1) exhibited weak photocatalytic activity likely due to a "shading effect", while nanocomposites (*x*:1 CN) showed enhanced photocatalytic activity that can be ascribed to the effective establishment of heterojunctions. Moreover, g-C_3N_4/ZnO nanocomposites (*x*:1 CN) demonstrated high stability, retaining its initial activity after repeated cycles. This work reveals a facile two-step in-situ synthesis method to prepare g-C_3N_4 based hybrid materials that are promising for industrial scale applications.

Supplementary Materials: The following are available online at http://www.mdpi.com/2079-4991/9/2/215/s1, Figure S1: N_2 adsorption-desorption isotherms; Figure S2: N_2 adsorption-desorption isotherms for three representative nanocomposites; Figure S3: XRD patterns for fresh and ultrasonically treated 0.1:1 CN nanocomposite.

Author Contributions: Conceptualization: C.S. and M.L. experimental design: S.Z., H.R.; experiments: S.G.; validation: L.Z., M.W., Z.Z.; formal analysis: M.L., L.L. and X.C.; writing—original draft preparation: M.L.; writing—review and editing: C.S., L.L.; supervision: X.C.

Funding: This research was funded by the National Natural Science Foundation of China (51702126, 21802053, 21503092), the Start-up Fund (70516036) and Student Research Training Program (85178564) of Jiaxing University, Zhejiang Provincial Natural Science Foundation of China (LY19B030005).

Conflicts of Interest: The authors declare no conflict of interest.

References

1. Izumi, Y. Recent advances in the photocatalytic conversion of carbon dioxide to fuels with water and/or hydrogen using solar energy and beyond. *Coord. Chem. Rev.* **2013**, *257*, 171–186. [CrossRef]
2. Zhong, H.; Zhang, Q.; Wang, J.; Zhang, X.; Wei, X.; Wu, Z.; Li, K.; Meng, F.; Bao, D.; Yan, J. Engineering Ultrathin C_3N_4 Quantum Dots on Graphene as a Metal-Free Water Reduction Electrocatalyst. *ACS Catal.* **2018**, *8*, 3965–3970. [CrossRef]
3. Wang, Y.; Liu, X.; Liu, J.; Han, B.; Hu, X.; Yang, F.; Xu, Z.; Li, Y.; Jia, S.; Li, Z.; et al. Carbon Quantum Dot Implanted Graphite Carbon Nitride Nanotubes: Excellent Charge Separation and Enhanced Photocatalytic Hydrogen Evolution. *Angew. Chem. Int. Ed.* **2018**, *130*, 5867–5873. [CrossRef]

4. Park, B.-G. Photocatalytic Behavior of Strontium Aluminates Co-Doped with Europium and Dysprosium Synthesized by Hydrothermal Reaction in Degradation of Methylene Blue. *Catalysts* **2018**, *45*, 227–236. [CrossRef]
5. Sun, M.; Senthil, R.; Pan, J.; Osman, S.; Khan, A. A Facile Synthesis of Visible-Light Driven Rod-on-Rod like α-FeOOH/α-$AgVO_3$ Nanocomposite as Greatly Enhanced Photocatalyst for Degradation of Rhodamine B. *Catalysts* **2018**, *8*, 392. [CrossRef]
6. Yin, G.; Huang, X.; Chen, T.; Zhao, W.; Bi, Q.; Xu, J.; Han, Y.; Huang, F. Hydrogenated Blue Titania for Efficient Solar to Chemical Conversions: Preparation, Characterization, and Reaction Mechanism of CO_2 Reduction. *ACS Catal.* **2018**, *8*, 1009–1017. [CrossRef]
7. Zhu, Y.; Gao, C.; Bai, S.; Chen, S.; Long, R.; Song, L.; Li, Z.; Xiong, Y. Hydriding Pd cocatalysts: An approach to giant enhancement on photocatalytic CO_2 reduction into CH_4. *Nano Res.* **2017**, *10*, 3396–3406. [CrossRef]
8. Yan, Y.; Crisp, R.W.; Gu, J.; Chernomordik, B.D.; Pach, G.F.; Marshall, A.R.; Turner, J.A.; Beard, M.C. Multiple exciton generation for photoelectrochemical hydrogen evolution reactions with quantum yields exceeding 100%. *Nat. Energy* **2017**, *2*, 17052–17058. [CrossRef]
9. Wang, W.; Yu, J.C.; Xia, D.; Wong, P.K.; Li, Y. Graphene and g-C_3N_4 nanosheets cowrapped elemental alpha-sulfur as a novel metal-free heterojunction photocatalyst for bacterial inactivation under visible-light. *Environ. Sci. Technol.* **2013**, *47*, 8724–8732. [CrossRef]
10. Wang, J.; Yang, Z.; Gao, X.; Yao, W.; Wei, W.; Chen, X.; Zong, R.; Zhu, Y. Core-shell g-C_3N_4@ZnO composites as photoanodes with double synergistic effects for enhanced visible-light photoelectrocatalytic activities. *Appl. Catal. B Environ.* **2017**, *217*, 169–180. [CrossRef]
11. Stassi, S.; Cauda, V.; Ottone, C.; Chiodoni, A.; Pirri, C.F.; Canavese, G. Flexible piezoelectric energy nanogenerator based on ZnO nanotubes hosted in a polycarbonate membrane. *Nano Energy* **2015**, *13*, 474–481. [CrossRef]
12. Guo, Y.; Wang, H.; He, C.; Qiu, L.; Cao, X. Uniform Carbon-Coated ZnO Nanorods: Microwave-Assisted Preparation, Cytotoxicity, and Photocatalytic Activity. *Langmuir* **2009**, *25*, 4678–4684. [CrossRef] [PubMed]
13. Zhang, Y.; Liu, Y.; Zhou, L.; Liu, D.; Liu, F.; Liu, F.; Liang, X.; Yan, X.; Gao, Y.; Lu, G. The role of Ce doping in enhancing sensing performance of ZnO-based gas sensor by adjusting the proportion of oxygen species. *Sens. Actuators B Chem.* **2018**, *273*, 991–998. [CrossRef]
14. Vaiano, V.; Iervolino, G.; Rizzo, L. Cu-doped ZnO as efficient photocatalyst for the oxidation of arsenite to arsenate under visible light. *Appl. Catal. B Environ.* **2018**, *238*, 471–479. [CrossRef]
15. Wei, C.; Liu, W.; Chen, Q.; Hou, H.; Liu, C.; Hou, C.; Xiong, W.; Zhang, D. Nitrogen-doped ZnO/Carbon hollow rhombic dodecahedral for photoelectrochemical sensing glutathione. *Appl. Surf. Sci.* **2018**, *458*, 872–879. [CrossRef]
16. Liang, X.; Shi, X.; Zhang, F.; Li, Y.; Zhang, H.; Yuan, Y. Improved H_2 Production by Ethanol Steam Reforming over Sc_2O_3-Doped Co-ZnO Catalysts. *Catalysts* **2017**, *7*, 241. [CrossRef]
17. Hong, D.; Cao, G.; Zhang, X.; Qu, J.; Deng, Y.; Liang, H.; Tang, J. Construction of a Pt-modified chestnut-shell-like ZnO photocatalyst for high-efficiency photochemical water splitting. *Electrochim. Acta* **2018**, *283*, 959–969. [CrossRef]
18. Zhang, H.; Sun, J.; Dagle, V.L.; Halevi, B.; Datye, A.K.; Wang, Y. Influence of ZnO Facets on Pd/ZnO Catalysts for Methanol Steam Reforming. *ACS Catal.* **2014**, *4*, 2379–2386. [CrossRef]
19. Jo, W.K.; Selvam, N.C.S. Enhanced visible light-driven photocatalytic performance of ZnO-g-C_3N_4 coupled with graphene oxide as a novel ternary nanocomposite. *J. Hazard. Mater.* **2015**, *299*, 462–470. [CrossRef]
20. Zheng, L.; Zheng, Y.; Chen, C.; Zhan, Y.; Lin, X.; Zheng, Q.; Wei, K.; Zhu, J. Network Structured SnO_2/ZnO Heterojunction Nanocatalyst with High Photocatalytic Activity. *Inorg. Chem.* **2009**, *48*, 1819–1825. [CrossRef]
21. Wang, L.; Ma, C.; Guo, Z.; Lv, Y.; Chen, W.; Chang, Z.; Yuan, Q.; Ming, H.; Wang, J. In-situ growth of g-C_3N_4 layer on ZnO nanoparticles with enhanced photocatalytic performances under visible light irradiation. *Mater. Lett.* **2017**, *188*, 347–350. [CrossRef]
22. Li, M.; Zhang, L.; Wu, M.; Du, Y.; Fan, X.; Wang, M.; Zhang, L.; Kong, Q.; Shi, J. Mesostructured CeO_2/g-C_3N_4 nanocomposites: Remarkably enhanced photocatalytic activity for CO_2 reduction by mutual component activations. *Nano Energy* **2016**, *19*, 145–155. [CrossRef]
23. Tian, J.; Zhang, L.; Wang, M.; Jin, X.; Zhou, Y.; Liu, J.; Shi, J. Remarkably enhanced H_2 evolution activity of oxidized graphitic carbon nitride by an extremely facile K_2CO_3-activation approach. *Appl. Catal. B Environ.* **2018**, *232*, 322–329. [CrossRef]

24. Cao, S.; Low, J.; Yu, J.; Jaroniec, M. Polymeric photocatalysts based on graphitic carbon nitride. *Adv. Mater.* **2015**, *27*, 2150–2176. [CrossRef] [PubMed]
25. Su, F.; Mathew, S.; Lipner, G.; Fu, X.; Antonietti, M.; Blechert, S.; Wang, X. mpg-C_3N_4-catalyzed selective oxidation of alcohols using O_2 and visible light. *J. Am. Chem. Soc.* **2010**, *132*, 16299–16301. [CrossRef] [PubMed]
26. Yuan, X.; Duan, S.; Wu, G.; Sun, L.; Cao, G.; Li, D.; Xu, H.; Li, Q.; Xia, D. Enhanced catalytic ozonation performance of highly stabilized mesoporous ZnO doped g-C_3N_4 composite for efficient water decontamination. *Appl. Catal. A-Gen.* **2018**, *551*, 129–138. [CrossRef]
27. Wang, Y.J.; Shi, R.; Zhu, Y. Enhancement of photocurrent and photocatalytic activity of ZnO hybridized with graphite-like C_3N_4. *Energy Eviron. Sci.* **2011**, *4*, 2922–2929. [CrossRef]
28. Liu, W.; Wang, M.L.; Xu, C.; Chen, S.; Fu, X. Significantly enhanced visible-light photocatalytic activity of g-C_3N_4 via ZnO modification and the mechanism study. *J. Mol. Catal. A Chem.* **2013**, *368*, 9–15. [CrossRef]
29. Zhu, Y.; Li, M.; Liu, Y.; Ren, T.; Yuan, Z. Carbon-Doped ZnO Hybridized Homogeneously with Graphitic Carbon Nitride Nanocomposites for Photocatalysis. *J. Phys. Chem. C* **2014**, *118*, 10963–10971. [CrossRef]
30. Park, T.J.; Pawar, R.C.; Kang, S.; Lee, C.S. Ultra-thin coating of g-C_3N_4 on an aligned ZnO nanorod film for rapid charge separation and improved photodegradation performance. *RSC Adv.* **2016**, *6*, 89944–89952. [CrossRef]
31. Hu, Z.; Wang, L.; Zhang, K.; Wang, J.; Cheng, F.; Tao, Z.; Chen, J. MoS_2 Nanoflowers with Expanded Interlayers as High-Performance Anodes for Sodium-Ion Batteries. *Angew. Chem. Int. Ed.* **2014**, *53*, 12794–12798. [CrossRef]
32. Hou, Y.; Laursen, A.B.; Zhang, J.; Zhang, G.; Zhu, Y.; Wang, X.; Dahl, S.; Chorkendorff, I. Layered Nanojunctions for Hydrogen-Evolution Catalysis. *Angew. Chem. Int. Ed.* **2013**, *52*, 3621–3625. [CrossRef] [PubMed]
33. Shi, J. On the synergetic catalytic effect in heterogeneous nanocomposite catalysts. *Chem. Rev.* **2013**, *113*, 2139–2181. [CrossRef] [PubMed]
34. Zhang, X.; Qin, J.; Xue, Y.; Yu, P.; Zhang, B.; Wang, L.; Liu, R. Effect of aspect ratio and surface defects on the photocatalytic activity of ZnO nanorods. *Sci. Rep.* **2014**, *4*, 4596–4603. [CrossRef] [PubMed]
35. Li, M.; Zhang, L.; Fan, X.; Zhou, Y.; Wu, M.; Shi, J. Highly selective CO_2 photoreduction to CO over g-C_3N_4/Bi_2WO_6 composites under visible light. *J. Mater. Chem. A* **2015**, *3*, 5189–5196. [CrossRef]
36. Wang, X.; Maeda, K.; Thomas, A.; Takanabe, K.; Xin, G.; Carlsson, J.M.; Domen, K.; Antonietti, M. A metal-free polymeric photocatalyst for hydrogen production from water under visible light. *Nat. Mater.* **2009**, *8*, 76–80. [CrossRef] [PubMed]
37. Sun, Z.; Guo, J.; Zhu, S.; Mao, L.; Ma, J.; Zhang, D. A high-performance Bi_2WO_6-graphene photocatalyst for visible light-induced H_2 and O_2 generation. *Nanoscale* **2014**, *6*, 2186–2193. [CrossRef]
38. Yoon, M.; Seo, M.; Jeong, C.; Jang, J.H.; Jeon, K.S. Synthesis of Liposome-Templated Titania Nanodisks: Optical Properties and Photocatalytic Activities. *Chem. Mater.* **2005**, *17*, 6069–6079. [CrossRef]
39. Wang, X.; Blechert, S.; Antonietti, M. Polymeric Graphitic Carbon Nitride for Heterogeneous Photocatalysis. *ACS Catal.* **2012**, *2*, 1596–1606. [CrossRef]
40. Djurišić, A.B.; Choy, W.C.H.; Roy, V.A.L.; Leung, Y.H.; Kwong, C.Y.; Cheah, K.W.; Rao, T.K.G.; Chan, W.K.; Lui, H.F.; Surya, C. Photoluminescence and Electron Paramagnetic Resonance of ZnO Tetrapod Structures. *Adv. Funct. Mater.* **2004**, *14*, 856–864. [CrossRef]
41. Chang, C.; Fu, Y.; Hu, M.; Wang, C.; Shan, G.; Zhu, L. Photodegradation of bisphenol A by highly stable palladium-doped mesoporous graphite carbon nitride (Pd/mpg-C_3N_4) under simulated solar light irradiation. *Appl. Catal. B Environ.* **2013**, *142–143*, 553–560. [CrossRef]
42. Zheng, J.H.; Jiang, Q.; Lian, J.S. Synthesis and optical properties of flower-like ZnO nanorods by thermal evaporation method. *Appl. Surf. Sci.* **2011**, *257*, 5083–5087. [CrossRef]
43. Cao, S.; Shen, B.; Tong, T.; Fu, J.; Yu, J. 2D/2D Heterojunction of ultrathin MXene/Bi_2WO_6 nanosheets for improved photocatalytic CO_2 reduction. *Adv. Funct. Mater.* **2018**, *28*, 1800136. [CrossRef]
44. Gao, D.; Xu, Q.; Zhang, J.; Yang, Z.; Si, M.; Yan, Z.; Xue, D. Defect-related ferromagnetism in ultrathin metal-free g-C_3N_4 nanosheets. *Nanoscale* **2014**, *6*, 2577–2581. [CrossRef] [PubMed]
45. Liu, C.; Jing, L.; He, L.; Luan, Y.; Li, C. Phosphate-modified graphitic C_3N_4 as efficient photocatalyst for degrading colorless pollutants by promoting O_2 adsorption. *Chem. Commun.* **2014**, *50*, 1999–2001. [CrossRef] [PubMed]

46. Li, K.; Gao, S.; Wang, Q.; Xu, H.; Wang, Z.; Huang, B.; Dai, Y.; Lu, J. In-Situ-Reduced Synthesis of Ti^{3+} Self-Doped TiO_2/g-C_3N_4 Heterojunctions with High Photocatalytic Performance under LED Light Irradiation. *ACS Appl. Mater. Interfaces* **2015**, *7*, 9023–9030. [CrossRef]
47. Yang, X.; Qian, F.; Zou, G.; Li, M.; Lu, J.; Li, Y.; Bao, M. Facile fabrication of acidified g-C_3N_4/g-C_3N_4 hybrids with enhanced photocatalysis performance under visible light irradiation. *Appl. Catal. B Environ.* **2016**, *193*, 22–35. [CrossRef]
48. An, H.; Su, C.; McGinn, P.J. Application of potash glass as a catalyst for diesel soot oxidation. *Catal. Commun.* **2009**, *10*, 509–512. [CrossRef]
49. Su, C.; McGinn, P.J. The effect of Ca^{2+} and Al^{3+} additions on the stability of potassium disilicate glass as a soot oxidation catalyst. *Appl. Catal. B Environ.* **2013**, *138*, 70–78. [CrossRef]
50. Su, C.; McGinn, P.J. Application of glass soot catalysts on metal supports to achieve low soot oxidation temperature. *Catal. Commun.* **2014**, *43*, 1–5. [CrossRef]
51. Su, C. Stabilization of Potassium in Soot Oxidation Catalysts and Their Application on Diesel Particulate Filters. Ph.D. Thesis, University of Notre Dame, Notre Dame, IN, USA, 2011.
52. Chen, X.; Kumar, A.; Klippstein, D.; Stafford, R.; Su, C.; Yuan, Y.; Zokoe, J.; McGinn, P. *Development and Demonstration of a Soot Generator Integrated Bench Reactor*; SAE Technical Paper 2014-01-1589; SAE: Warrendale, PA, USA, 2014.
53. McGinn, P.J.; Su, C. Glass Catalysts for Soot Combustion and Methods of Manufacturing the Same. U.S. Patent 9,592,490, 14 March 2017.
54. Su, C.; Wang, Y.; Kumar, A.; McGinn, P.J. Simulating real world soot-catalyst contact conditions for lab-scale catalytic soot oxidation studies. *Catalysts* **2018**, *8*, 247. [CrossRef]
55. Liu, Y.; Su, C.; Clerc, J.; Harinath, A.; Rogoski, L. Experimental and Modeling Study of Ash Impact on DPF Backpressure and Regeneration Behaviors. *SAE Int. J. Eng.* **2015**, *8*, 1313–1321. [CrossRef]
56. Su, C.; DeHart, T.; Anderson, M.; McGinn, P.J. Structured glass catalytic coating on wire mesh for particulate matter (PM) removal by modified sol-gel processing. *Mater. Lett.* **2019**, *234*, 168–171. [CrossRef]
57. Su, C.; Brault, J.; Munnannur, A.; Liu, Z.; Milloy, S.; Harinath, A.; Dunnuck, D.; Federle, K. *Model-Based Approaches in Developing an Advanced Aftertreatment System: An Overview*; SAE Technical Paper, 2019-01-0026; SAE: Warrendale, PA, USA, 2019.
58. Wang, Y.; Pan, Y.; Su, C.; Srinivasan, A.; Gong, J.; Kamp, C.J. Performance of Asymmetric Particulate Filter with Soot and Ash Deposits: Analytical Solution and Its Application. *Ind. Eng. Chem. Res.* **2018**, *57*, 15846–15856. [CrossRef]
59. Zhang, H.; Xi, Y.; Su, C.; Liu, Z.G. *Lab Study of Urea Deposit Formation and Chemical Transformation Process of Diesel Aftertreatment System*; SAE Technical Paper, 2017-01-0915; SAE: Warrendale, PA, USA, 2017.